

The Carnegie RR Lyrae Program: The Mid-Infrared RR Lyrae Period-Luminosity Relation in ω Cen and also metallicity

Meredith J. Durbin^{1,2*} Victoria Scowcroft³ Wendy Freedman⁴ Barry Madore³
 Rachael Beaton³ Andrew J. Monson⁵ Mark Seibert³

¹ Space Telescope Science Institute, 3700 San Martin Drive, Baltimore, MD 21218, USA

² Pomona College, Claremont, CA 91711, USA

³ Observatories of the Carnegie Institution of Washington, 813 Santa Barbara St., Pasadena, CA 91101, USA

⁴ Department of Astronomy and Astrophysics, University of Chicago, 5640 S Ellis Ave, Chicago, IL 60637, USA

⁵ Department of Astronomy and Astrophysics, The Pennsylvania State University, 403 Davey Lab, University Park, PA, 16802, USA

Accepted XXX. Received YYY; in original form ZZZ

ABSTRACT

Something something metallicity

Key words: keyword1 - keyword2 - keyword3

1 INTRODUCTION

The Carnegie RR Lyrae Program (CRRP) is a Warm *Spitzer* program (Freedman et al. 2012a, PID 90002) with the aim of calibrating the mid-infrared (mid-IR) RR Lyrae period-luminosity (PL) relation. Similar to the Carnegie Hubble Program (CHP) (Freedman et al. 2011), which used mid-IR observations of Cepheids to measure the Hubble constant (H_0 Freedman et al. 2012b), the results of the CRRP will be used to provide an independent, population II calibration of the zero-point of the extragalactic distance scale, and hence an independent measurement of H_0 .

In recent years it has become increasingly important to obtain independent direct measurements of H_0 . The results of Riess et al. (2011) and Freedman et al. (2012b), both which use Cepheids and type Ia supernovae (SNe), agree very well at 74.4 ± 2.5 km s⁻¹ Mpc⁻¹ and 74.3 ± 2.6 km s⁻¹ Mpc⁻¹, respectively. However, when we consider the latest results from *Planck*, who find 67.48 ± 0.98 km s⁻¹ Mpc⁻¹ (Planck Collaboration et al. 2015), there is tension. The *Planck* study derives their measurement from a model of the cosmic microwave background (CMB), so is completely independent of the Riess et al. and Freedman et al. results.

There have been several recent works that have investigated possible sources of uncertainty in the distance ladder that may contribute to the discrepancy between H_0 measurements. For example, Rigault et al. (2015) examine the differences in star formation rates in type Ia SNe host galaxies. They find that the intrinsic brightness of a SNe Ia may be affected by the local host environment; i.e. whether the SN occurs in a locally star forming or locally passive environment. Efsthathiou (2014) reanalysed the Cepheid data from Riess et al. (2011), and found that different outlier rejection criteria

lowered the resultant value of H_0 to 70.6 ± 3.3 km s⁻¹ Mpc⁻¹, making it compatible with the value from *Planck*.

The CRRP assesses a systematic that was unreachable in the original CHP – the intrinsic accuracy of the mid-IR Cepheid standard candle distance scale when compared to the standard ruler distance scale of the CMB and Baryon Acoustic Oscillation (BAO) measurements. With only one “test candle” it was impossible to make any assessment of this accuracy. However, with two standard candles with similar precision we can make meaningful comparisons and assess their systematic accuracy.

RR Lyrae variables (hereafter RRL) are intrinsically fainter than Cepheids, and in the optical follow a much shallower, even horizontal, PL relation (Catelan et al. 2004). Determining an accurate distance to an RRL in the V band requires knowledge of its metallicity. However, Longmore et al. (1986) showed that the true power of RRL as distance indicators lies in the IR passbands. Several groups have been studying the populations of RRL in globular clusters and nearby dwarf spheroidal galaxies (e.g. Garofalo et al. 2013; Ordoñez et al. 2014; Cusano et al. 2015; Kains et al. 2015, and references therein), and *HST* parallaxes were obtained for several Galactic RRL calibrators (Benedict et al. 2011). **Should we assume people will understand “calibrator” in this context? It took me a while to pick up on it**

Distance measurements made in the mid-IR benefit from reduced extinction effects, where $A_{[3.6]}$ and $A_{[4.5]}$ are 16 to 20 times lower than A_V Cardelli et al. (1989); Indebetouw et al. (2005). Additionally, the precision of distances obtained from the RRL PL relation is increased. At the wavelengths observed by Warm *Spitzer* (3.6 and 4.5 μ m) we do not see photospheric effects, but only the effects of temperature driving the pulsation; essentially, the mid-infrared light curve is tracing the change in radius of the star over a pulsation cycle. A by-product of this effect is that the intrinsic width of the RRL PL relation is also minimised in the mid-IR. The PL relation for pulsational variables can be thought of as a two-dimensional

* E-mail: mdurbin@stsci.edu

projection of the three-dimensional period-luminosity-colour relation (see figure 3 of [Madore & Freedman \(1991\)](#) for a graphical representation). As the colour-width decreases in the mid-IR, the width of the PL naturally decreases. As one moves from the optical to the mid-IR, the slope of the PL relation steepens and its dispersion dramatically decreases, and the slope should asymptotically approach the predicted slope of the period-radius relation, resulting in a slope between -2.4 and -2.8 , confirmed empirically by [Madore et al. \(2013\)](#). Through this decrease in dispersion we have found that the intrinsic width of the mid-IR PL for RRL is in fact smaller than for Cepheids -0.05 mag compared to 0.10 mag ([Neeley et al. 2015](#)). This translates to an uncertainty on an individual RR Lyrae star of 2%, compared to 4% for Cepheids.

In this work we focus on the effects of metallicity on the RR Lyrae (RRL) PL relation. Several Galactic Globular Clusters are being observed as part of CRRP, but ω Cen is unique in that it exhibits a measureable spread in metallicity ([Freeman & Rodgers 1975](#); [Villanova et al. 2007, 2014](#)).

There are very few metallic or molecular transition lines in the mid-IR at typical RRL temperatures, so the effects of metallicity on luminosity should be minimised. However, ω Cen provides the ideal test bed for any effect that we may not have predicted. Such an effect is not out of the realm of possibility; for example, the strength of the CO band head at $4.5 \mu\text{m}$ has been found to have a significant effect on Cepheid colours, and has such prevented the IRAC $4.5 \mu\text{m}$ Cepheid observations from being used for distance measurements in the CHP ([Scowcroft et al. 2011](#); [Monson et al. 2012](#); [Scowcroft et al. 2015](#)). As our concern in this program is systematic precision, we must ensure that similar effects do not plague the RRL distance scale.

The paper is set out as follows: Section 2 details the observations and data reduction. Section 3 presents the photometry of the ω Cen RRL. Section 4 describes the mid-IR PL relations and Section 5 discusses the application of these to a distance measurement of ω Cen. Section 6 examines the effects of metallicity on RRL magnitudes and distance estimates. Section 7 discusses the implications of this, and other systematic effects we consider in this work. In Section 8 we present our conclusions.

2 OBSERVATIONS & DATA REDUCTION

This work combines mid-IR observations from the Warm *Spitzer* mission, with supporting near-IR observations from the FourStar instrument on the Baade-Magellan telescope at Las Campanas Observatory ([Persson et al. 2013](#)). Figure 1 shows a K_s FourStar image with the *Spitzer* fields outlined, and the positions of known RRL plotted as circles.

2.1 Warm *Spitzer* Data

The Warm *Spitzer* observations for this work were taken as part of the Carnegie RR Lyrae Program. Three fields in ω Cen were chosen; their positions and the positions of known ω Cen RRLs are shown in Figure 1. To obtain optimal RRL light curves we observed each field 12 times over approximately 16 hours, roughly corresponding to the period of the longest period RRL we expected in the field. The observations of all three fields were taken on 2013 May 10 and 2013 May 11. Each field was observed using *Spitzer* IRAC ([Fazio et al. 2004](#)) with a 30s frame time with a medium scale, gaussian 5-point dither pattern to mitigate any image artefacts. Images were collected in both the 3.6 and $4.5 \mu\text{m}$ channels. The elongated field

shapes come from the design of IRAC; while the $[3.6]$ channel is collecting on-target data, the $[4.5]$ channel collects off target data “for free”, and vice versa. We chose to include these off-target fields to maximise the number of RRL in our final sample and to increase the legacy value of our data set to the community.

The science images were created using MOPEX ([Makovoz et al. 2006](#)), first running overlap correction on the basic calibrated data (cBCDs) then mosaicking them at 0.6 arcsec pixel scale using the drizzle algorithm. Mosaicked location-correction images were created at the same time.

PSF photometry was performed using DAOPHOT and ALLFRAME ([Stetson 1987, 1994](#)). The PSF model was created for each field/filter combination using the first epoch data. This was then applied to each other epoch. As the observations were taken temporally close together the effects of telescope rotation between epochs on the mosaicked PSF were minimal, so making a single good PSF model for each field/filter combination was much more efficient than creating one for every epoch.

Master star lists for ALLFRAME were created for each filter/field combination using a median mosaicked image created by MOPEX. We did not use the same single master star list for both filters as only a small proportion ($1/3$) of the $3.6 \mu\text{m}$ and $4.5 \mu\text{m}$ fields overlap each other. Instead we performed separate ALLFRAME reductions for each filter, and combined the results after the fact using DAOMATCH and DAOMASTER. Our mid-IR photometry is calibrated to the standard system set by [Reach et al. \(2005\)](#).

2.2 FourStar Data

J , H and K_s data were taken with the FourStar instrument on the Baade-Magellan telescope at Las Campanas Observatory ([Persson et al. 2013](#)) on the nights of 2013 June 25, 2013 June 27, and 2013 June 28. Four epochs were obtained each night in each filter for a total of 12 epochs. A mosaic of 5×3 (slightly overlapping) pointings (tiles) covered a 50×30 arcminute field of view centered on ω Cen. Each tile consists of a 5 point dither pattern with a 5.8 second exposure time. Stacked mosaics of the entire field were made as well as individual tiles using a customized pipeline for FourStar data. The purpose of the individual tiles is to provide photometry with better time resolution than the large mosaic.

PSF photometry of the tiles was performed using DAOPHOT and ALLFRAME ([Stetson 1987, 1994](#)). A PSF model was created for each epoch/tile/filter combination. A master star list for ALLFRAME was created from the final K_s mosaic and the multi-wavelength/epoch results were combined using DAOMATCH and DAOMASTER. Our final photometry is calibrated to the 2MASS standard system ([Skrutskie et al. 2006](#)).

2.3 Crowding

The primary limiting factor in the data is crowding: 77 RRLs out of the original catalog of 192 ([Kaluzny et al. 2004](#)) were rejected due to crowding. We compared the *Spitzer* images to the FourStar K_s -band image. The 0.159 arcsec/pixel resolution of the K_s band image enabled us to assess which stars were significantly contaminated. Our full, uncrowded RRL sample consists of 97 stars in J and H , 99 in K_s , 37 in $3.6 \mu\text{m}$, and 43 in $4.5 \mu\text{m}$.

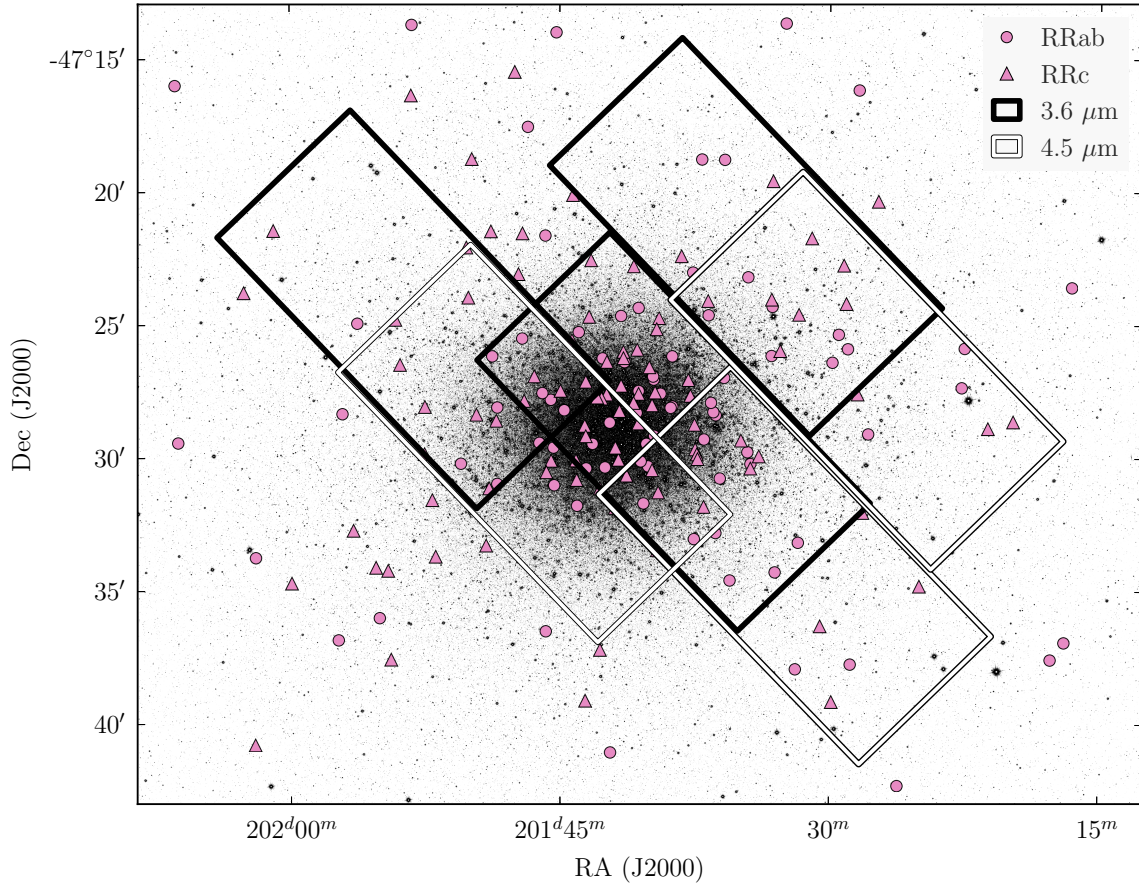


Figure 1. A K_s -band image of ω Cen from the FourStar camera, overlaid with a catalog of RRL from Kaluzny et al. (2004) and footprints of the *Spitzer* IRAC fields.

3 RESULTS

Our final photometry catalog, including magnitudes and uncertainties for JHK_s , [3.6], and [4.5], is presented in Table A1. The average magnitudes presented in Table A1 are flux averages, and the photometric uncertainties of the time series data are the error on the mean.

Our full, uncrowded RRL sample consists of 96 stars in J and H , 98 in K_s , 36 in [3.6], and 43 in [4.5]. For the PL fitting, detailed in the next section, we use only the stars for which we have photometry in all five bandpasses, ensuring that the same range of periods and metallicities are sampled for each wavelength. Our final RRL sample consists of 24 stars, or 12 in each pulsation mode.

4 PERIOD-LUMINOSITY RELATIONS

We use the theoretical near-infrared PL relation parameters presented in Marconi et al. (2015) for the JHK bands, and the empirical PL relation parameters derived from photometry of RRLs in the globular cluster M4 (NGC 6121) from Neeley et al. (2015) for the

IRAC bands. With the use of preexisting PL relation coefficients, the distance modulus becomes the only free parameter in our fit. We fit all distance moduli using an unweighted least-squares method, and fit the distance modulus to each pulsation mode in each wavelength separately.

For the mid-IR we use the PL relations from Neeley et al. (2015), as described in Table 2. These relations take the form

$$M = a + b \times (\log(P) + P_0) \quad (1)$$

where a and b are empirically derived coefficients and P_0 is the absolute value of the logarithm of the mean period of the M4 RRL sample. We calculate the PL zero-points assuming Neeley et al.'s M4 distance modulus of $\mu = 11.399$ mag.

The JHK RRL PL relations are described in Table 1. The relations take the form

$$M = a + b \times \log P + c \times [\text{Fe}/\text{H}] \quad (2)$$

where a , b , and c are theoretically derived coefficients.

The theoretical PL relations for the near-IR have a metallicity-dependent term; however, we do not have known metallicities for

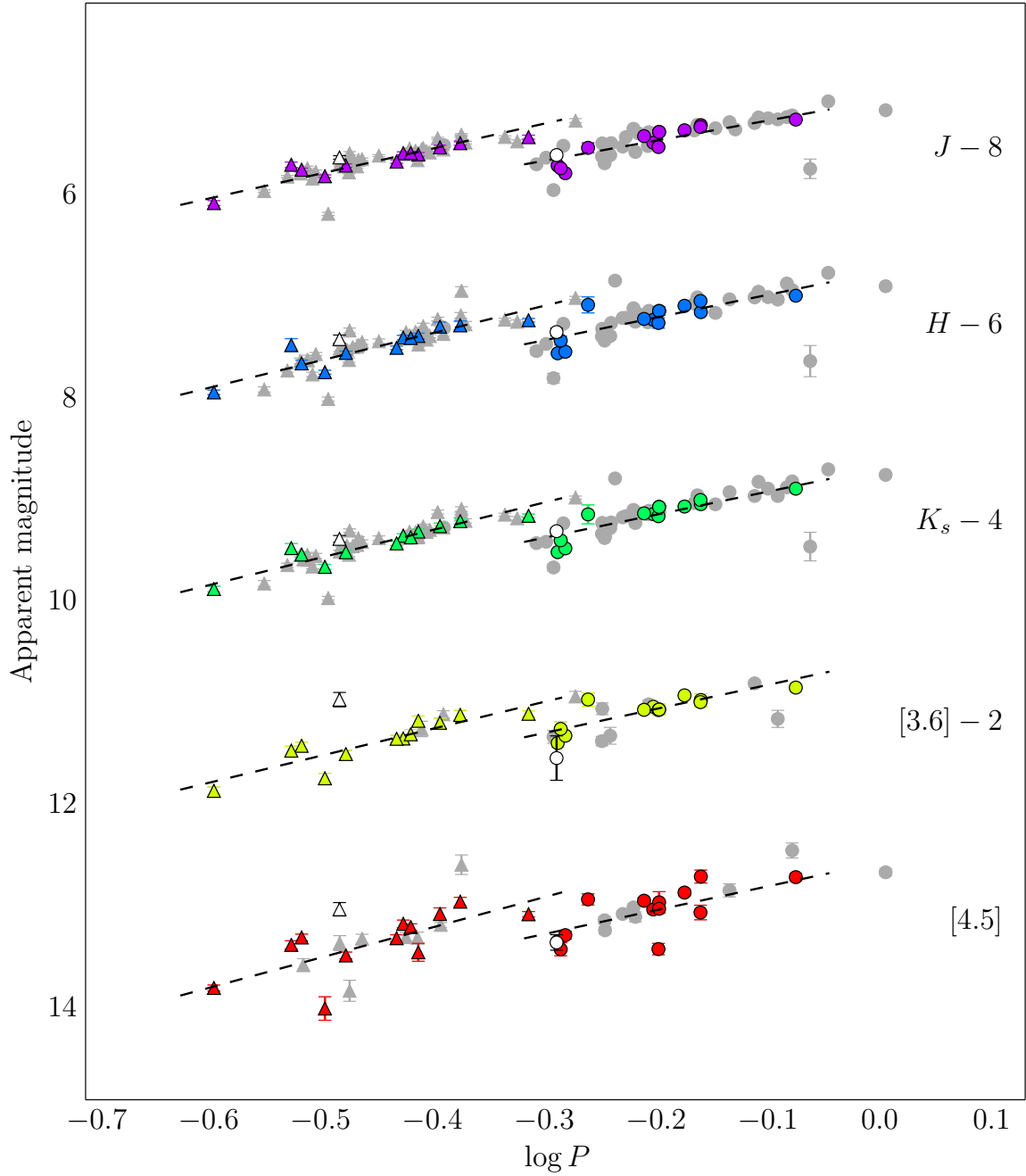


Figure 2. PL relations for JHK_s , $[3.6]$, and $[4.5]$ photometry assuming $[\text{Fe}/\text{H}] = -1.567$. Here circles represent RRab stars, triangles represent RRCs, colored points are the final consistent sample, grey points are stars that did not appear in all bands, and the unfilled points are stars rejected from the final sample based on 2σ clipping of the residuals of $3.6\ \mu\text{m}$ vs. the residuals of H and K .

all RRL in our sample. We therefore use the average $[\text{Fe}/\text{H}]$ of the RRLs for which there are known metallicities. Using spectroscopic metallicities from Sollima et al. (2006), we obtain an average $[\text{Fe}/\text{H}]$ of -1.567 . The effect of our choice of mean abundance is discussed further in Section 6.

5 DISTANCE MODULI

We combine the uncorrected distance moduli from each bandpass to obtain a mean reddening-corrected distance modulus. We fit the near-infrared reddening law from Cardelli et al. (1989) and mid-infrared law from Indebetouw et al. (2005) simultaneously, assuming a ratio of total to selective absorption $R_V = 3.1$. The resulting fit is shown in Figure 3. We derive a dereddened distance

Table 1. Theoretical near-IR RRL period-luminosity relation coefficients for ω Cen (Marconi et al. 2015), for relations of the form $M = a + b \times \log P + c \times [\text{Fe}/\text{H}]$ with predicted dispersion σ .

Band	Mode	a	b	c	σ
J	RRab	-0.510	-1.980	0.170	0.060
	RRc	-1.070	-2.460	0.150	0.040
H	RRab	-0.760	-2.240	0.190	0.040
	RRc	-1.310	-2.700	0.160	0.020
K_s	RRab	-0.820	-2.270	0.180	0.030
	RRc	-1.370	-2.720	0.150	0.020

Table 2. Empirical mid-IR RRL period-luminosity relation coefficients for ω Cen (Neeley et al. 2015), for relations of the form $M = a + b \times (\log(P) + P_0)$ with measured dispersion σ .

Band	Mode	a	b	P_0	σ
[3.6]	RRab	-0.558	-2.370	0.260	0.035
	RRc	-0.192	-2.658	0.550	0.021
[4.5]	RRab	-0.593	-2.355	0.260	0.036
	RRc	-0.240	-2.979	0.550	0.021

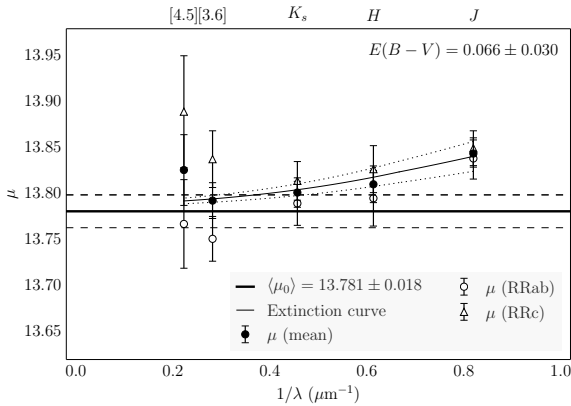


Figure 3. Distance moduli for the final sample of JHK_s , $3.6 \mu\text{m}$, and $4.5 \mu\text{m}$ photometry. The filled circles are the mean distance moduli using both RRab and RRc stars, the unfilled circles are the distance moduli using only RRab stars, and the filled triangles are distance moduli using only RRc stars. The reddening laws are fit to the mean distance moduli.

modulus of $\langle \mu_0 \rangle = 13.781 \pm 0.018$ with $E(B - V) = 0.066 \pm 0.030$ using the weighted mean RRab + RRc distances.

It is apparent from Figure 3 that there are large discrepancies in the distance moduli in 3.6 and $4.5 \mu\text{m}$ for the two pulsation modes; these contribute to the relatively low $E(B - V)$ value and high dereddened distance modulus. If we remove the RRc's and fit the extinction curve only to the RRab's, as shown in Figure 4, we obtain a better fit of all points to the extinction curve than when we use the mean. From these distance moduli we derive a dereddened distance modulus of $\langle \mu_0 \rangle = 13.739 \pm 0.024$ with $E(B - V) = 0.110 \pm 0.042$, both of which are closer to accepted values [CITE] than the values derived from the weighted mean distance moduli.

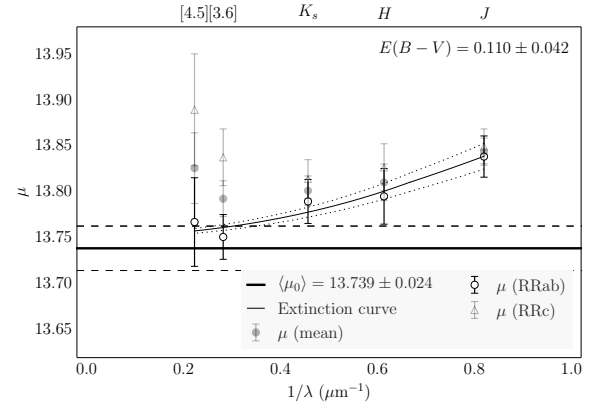


Figure 4. Distance moduli for the final sample of JHK_s , $3.6 \mu\text{m}$, and $4.5 \mu\text{m}$ photometry, with the reddening laws fit to the distances from RRab only.

6 METALLICITY

Theoretical models suggest that the metallicity dependence of the RRL PL relation should decrease monotonically from the optical to the near-infrared (Bono et al. 2001; Catelan et al. 2004). Observational evidence corroborates this; previous investigations performed on WISE data suggest no obvious metallicity dependence in the mid-IR PL relations (Madore et al. 2013).

ω Cen is ideal for examining the RRL period-luminosity-metallicity relation, because **need source for canonical metallicity spread** A metallicity spread this wide is not found in any other Galactic globular cluster. One of the advantages of using globular clusters to calibrate PL coefficients is that all stars in a cluster can be considered to be at the same distance from Earth. We can therefore assume that any dispersion in the PL relation is a combination of the a) the intrinsic dispersion of the PL relation, b) the photometric uncertainties, and c) dispersion induced by the spread in metallicity of the RRL. Since we have measured the intrinsic dispersion of the RRL PL in [3.6] and [4.5] from the cluster M4, Neeley et al. (2015) and our photometric uncertainties are well understood, the only unknown in this problem is the dispersion due to the spread in metallicity of the cluster.

We know from mid-IR spectra that a significant CO feature sits within the IRAC [4.5] filter. In the case of Cepheids, Scowcroft et al. (2011) and Scowcroft et al. (2015) have shown that this has a significant effect on the [4.5] magnitudes, and is metallicity dependent. However, this effect increases with decreasing temperatures, turning off completely above 6000 K where all the CO has been destroyed (Monson et al. 2012). As even the coolest RRL have temperatures over 6000 K (Iben 1971), we expect to see no such CO absorption in the [4.5] PL relation. If there are any other unanticipated metallicity effects for RRL, they must be smaller than the dispersion of the PL relations themselves, but we must still perform empirical tests to search for such effects.

We can place an upper limit on the contribution of metallicity to the measured PL dispersion by combining the probability distributions of the known intrinsic PL width and the scatter induced by photometric error and comparing the result to the observed distribution of ω Cen PL residuals. The following description of the process uses the RRab PL relation in [3.6] as the example case; we apply this method to both pulsation modes in both IRAC filters. We model the intrinsic scatter as a uniform distribution with a full width of

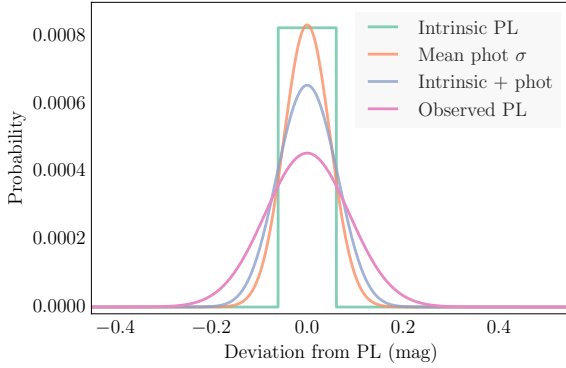


Figure 5. Probability distributions for components of PL scatter, with intrinsic width in green, photometric error in orange, the combination thereof in purple, and the observed distribution in pink.

Table 3. Some metallicity shift

Band	Mode	σ	γ , spect	γ , phot	
[3.6]	RRab	0.064	-1.980	0.282	0.234
[3.6]	RRc	0.091	0.778	0.190	0.323
[4.5]	RRab	0.162	0.712	0.180	0.590
[4.5]	RRc	0.195	1.660	0.180	0.689

$\sqrt{12}$ times the intrinsic PL width (see Table 2), $\sqrt{12} \times 0.035 = 0.121$ mag and the photometric uncertainties as a Gaussian distribution with a standard deviation of the mean photometric error in the sample, $\sigma = 0.048$ mag. We model the probability distribution of the observed PL residuals as a Gaussian centered at zero with a scale of the standard deviation of the residuals, $\sigma = 0.088$ mag. These models are shown in Figure 5, as well as the convolution of the intrinsic scatter and photometric error distributions.

To constrain the contribution of metallicity to the observed scatter, we model the metallicity-induced scatter as another Gaussian centered at zero. To find the standard deviation of this model, we convolve the metallicity distribution with the previous convolution of the intrinsic width and photometric error distributions, and minimize the difference between that and the observed distribution. For RRab's in [3.6], we find the standard deviation of the model metallicity distribution to be $\sigma = 0.064$.

Probably will be removed but should be discussed: Dividing the standard deviation of the metallicity distribution by the standard deviation of the metallicity, we find a γ parameter ($\gamma = \Delta \text{mag} / \Delta [\text{Fe}/\text{H}]$) of 0.282 using spectroscopic metallicities and 0.234 using photometric. Is this meaningful? Probably not! But here's a table of them just in case:

ω Cen is unique in that we can also take a second approach to establishing the metallicity effect on the RRL PL relation. As it is such an interesting system, ω Cen is extremely well studied and many of its RRL have spectroscopic or photometric metallicities in the literature (e.g. Sollima et al. 2006; Rey et al. 2000). As another test of the effect of metallicity, we use these measurements to assess the γ parameter for ω Cen, where

$$\gamma = \frac{\Delta \text{mag}}{[\text{Fe}/\text{H}]}, \quad (3)$$

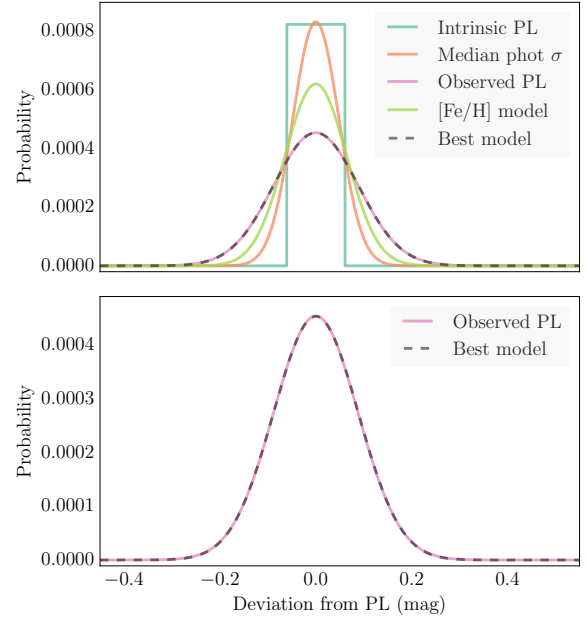


Figure 6. Top: Intrinsic, photometric error, and observed PL relations as in Figure 5, as well as the scaled metallicity distribution and best model (convolution of intrinsic, photometric, and metallicity distributions). Bottom: only the observed and model distributions for easier comparison.

Band	[Fe/H] type	γ	σ_γ	P_0	σ
[3.6]	Spectroscopic	-0.558	-2.370	0.260	0.035
	Photometric	-0.192	-2.658	0.550	0.021
[4.5]	Spectroscopic	-0.593	-2.355	0.260	0.036
	Photometric	-0.240	-2.979	0.550	0.021

similar to γ used to quantify the effect of metallicity on the zero-point of the Cepheid PL relation (Kennicutt et al. 1998).

If there is any correlation between $[\text{Fe}/\text{H}]$ and the PL residuals, we expect it to be a linear one, consistent with the theoretical metallicity terms in the PL relation, $c \times [\text{Fe}/\text{H}]$; we fit a relation of the form

$$\Delta \text{mag} = \gamma \times [\text{Fe}/\text{H}] + d \quad (4)$$

to the 3.6 μm and 4.5 μm PL residuals and metallicity values for stars with known individual metallicity values, as shown in Figure 7. By this metric we find that although the scatter in the 3.6 μm and 4.5 μm PL relations is higher for ω Cen than it is for M4 (Neeley et al. 2015; Braga et al. 2015), there is little evidence that it is due to metallicity. When we examine $[\text{Fe}/\text{H}]$ vs. the residuals of each PL relation, γ is within 1σ of zero for all fits, indicating that there is no significant metallicity dependence in the PL residuals.

7 DISCUSSION

Results from the *GAIA* mission (Lindgren & Perryman 1996) are expected to improve the characterization of the RRL PL relation dramatically. Trigonometric parallaxes and spectrophotometric metallicities of Galactic RRLs from *GAIA* will increase the number of calibrators for the absolute RRL PL relations by an order of mag-

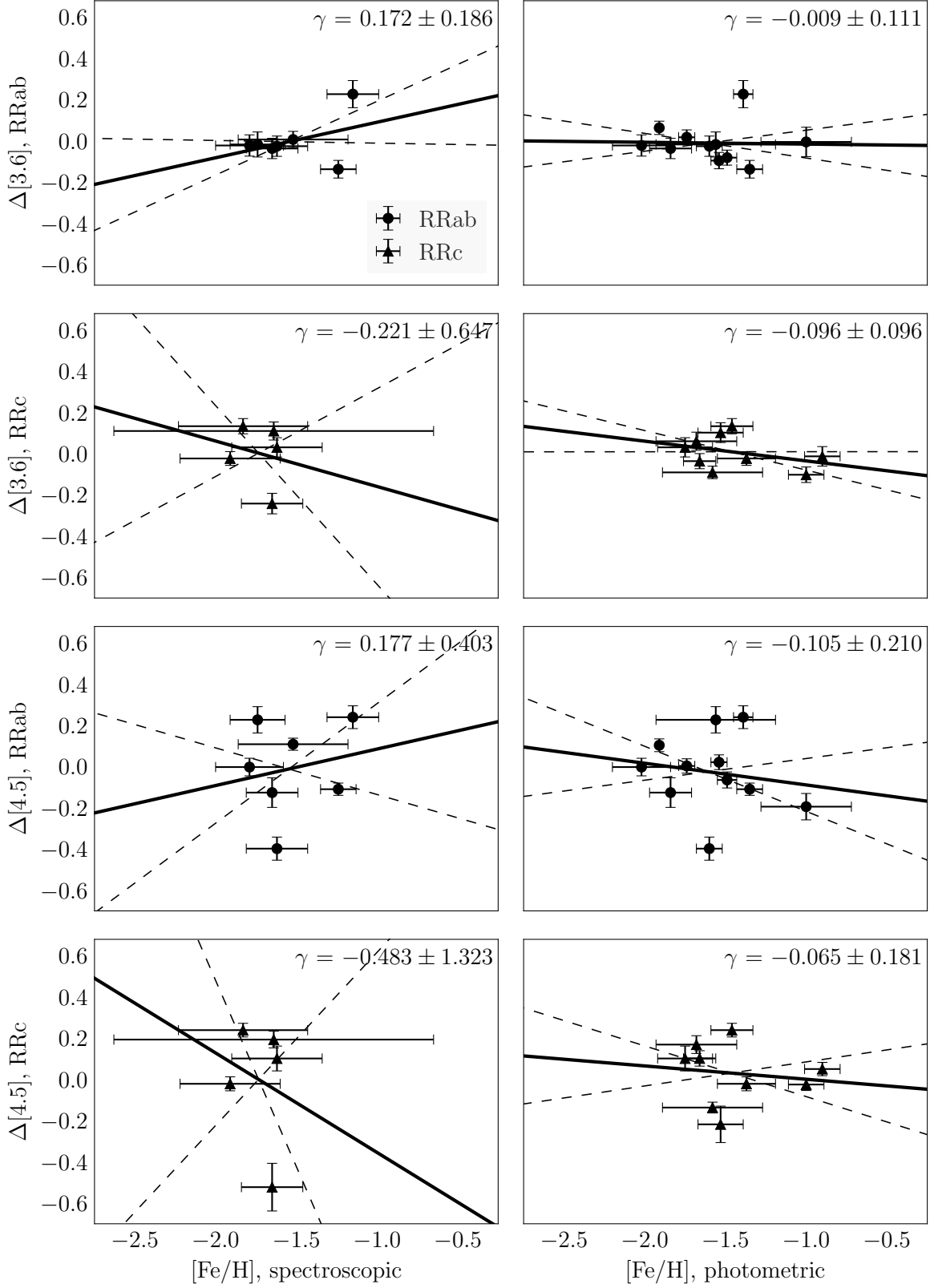


Figure 7. Photometric and spectroscopic $[\text{Fe}/\text{H}]$ values vs. period-luminosity residuals in 3.6 μm and 4.5 μm , with the γ parameter from equation 4 in the top right corner of each subplot.

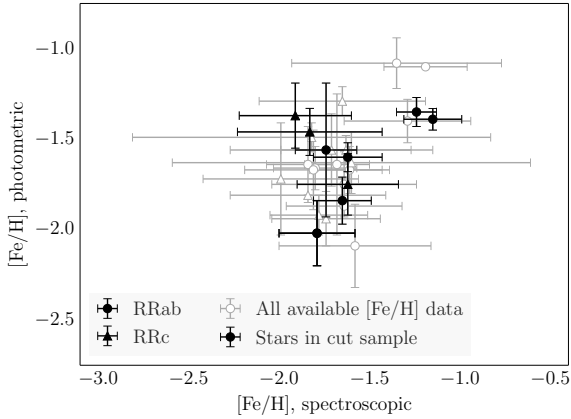


Figure 8. Spectroscopic vs. photometric measurements of $[\text{Fe}/\text{H}]$ for RRLs in ω Cen.

nitude (Liu et al. 2012, **overview paper**). [something about omega cen parallaxes and metallicities too]

We also anticipate that the NIRCcam instrument on *JWST* (Burriesci 2005; Gardner et al. 2006) will provide substantial improvements over IRAC for investigations of this nature. The NIRCcam filters F356W and F444W will provide data in passbands comparable to IRAC’s [3.6] and [4.5] at an order of magnitude higher resolution (0.065 arcsec/pixel), which will significantly decrease photometric error due to crowding and therefore allow us to obtain data for all known RRLs in ω Cen.

8 CONCLUSIONS

ACKNOWLEDGEMENTS

We thank Eric Persson for his many contributions to this project.

This work is based on observations made with the Spitzer Space Telescope, which is operated by the Jet Propulsion Laboratory, California Institute of Technology under a contract with NASA. Support for this work was provided by NASA through an award issued by JPL/Caltech.

This work was also supported in part by the Claremont-Carnegie Astrophysics Research Program.

This publication makes use of data products from the Two Micron All Sky Survey, which is a joint project of the University of Massachusetts and the Infrared Processing and Analysis Center/California Institute of Technology, funded by the National Aeronautics and Space Administration and the National Science Foundation.

This research has made use of the NASA/IPAC Extragalactic Database (NED), which is operated by the Jet Propulsion Laboratory, California Institute of Technology, under contract with the National Aeronautics and Space Administration.

REFERENCES

Benedict G. F., et al., 2011, *AJ*, **142**, 187
 Bono G., Caputo F., Castellani V., Marconi M., Storm J., 2001, *MNRAS*, **326**, 1183
 Braga V. F., et al., 2015, *ApJ*, **799**, 165

Burriesci L. G., 2005, in Heaney J. B., Burriesci L. G., eds, Society of Photo-Optical Instrumentation Engineers (SPIE) Conference Series Vol. 5904, Cryogenic Optical Systems and Instruments XI. pp 21–29, doi:10.1117/12.613596
 Cardelli J. A., Clayton G. C., Mathis J. S., 1989, *ApJ*, **345**, 245
 Catelan M., Pritzl B. J., Smith H. A., 2004, *ApJS*, **154**, 633
 Cusano F., et al., 2015, *ApJ*, **806**, 200
 Efsthathiou G., 2014, *MNRAS*, **440**, 1138
 Fazio G. G., et al., 2004, *ApJS*, **154**, 10
 Freedman W. L., et al., 2011, *AJ*, **142**, 192
 Freedman W., et al., 2012a, The Carnegie RR Lyrae Program, Spitzer Proposal
 Freedman W. L., Madore B. F., Scowcroft V., Burns C., Monson A., Persson S. E., Seibert M., Rigby J., 2012b, *ApJ*, **758**, 24
 Freeman K. C., Rodgers A. W., 1975, *ApJ*, **201**, L71
 Gardner J. P., et al., 2006, *Space Sci. Rev.*, **123**, 485
 Garofalo A., et al., 2013, *ApJ*, **767**, 62
 Iben Jr. I., 1971, *PASP*, **83**, 697
 Indebetouw R., et al., 2005, *ApJ*, **619**, 931
 Ivezić Ž., Connolly A., VanderPlas J., Gray A., 2013, Statistics, Data Mining, and Machine Learning in Astronomy
 Kains N., et al., 2015, *A&A*, **578**, A128
 Kaluzny J., Olech A., Thompson I. B., Pych W., Krzemiński W., Schwarzenberg-Czerny A., 2004, *A&A*, **424**, 1101
 Kennicutt Jr. R. C., et al., 1998, *ApJ*, **498**, 181
 Lindegren L., Perryman M. A. C., 1996, *A&AS*, **116**, 579
 Liu C., Bailer-Jones C. A. L., Sordo R., Vallenari A., Borraero R., Luri X., Sartoretti P., 2012, *MNRAS*, **426**, 2463
 Longmore A. J., Fernley J. A., Jameson R. F., 1986, *MNRAS*, **220**, 279
 Madore B. F., Freedman W. L., 1991, *PASP*, **103**, 933
 Madore B. F., et al., 2013, *ApJ*, **776**, 135
 Makovoz D., Roby T., Khan I., Booth H., 2006, in Society of Photo-Optical Instrumentation Engineers (SPIE) Conference Series. p. 0, doi:10.1117/12.672536
 Marconi M., et al., 2015, *ApJ*, **808**, 50
 Monson A. J., Freedman W. L., Madore B. F., Persson S. E., Scowcroft V., Seibert M., Rigby J. R., 2012, *ApJ*, **759**, 146
 Neeley J. R., et al., 2015, preprint, (arXiv:1505.07858)
 Ordoñez A. J., Yang S.-C., Sarajedini A., 2014, *ApJ*, **786**, 147
 Persson S. E., et al., 2013, *PASP*, **125**, 654
 Planck Collaboration et al., 2015, preprint, (arXiv:1502.01589)
 Reach W. T., et al., 2005, *PASP*, **117**, 978
 Rey S.-C., Lee Y.-W., Joo J.-M., Walker A., Baird S., 2000, *AJ*, **119**, 1824
 Riess A. G., et al., 2011, *ApJ*, **730**, 119
 Rigault M., et al., 2015, *ApJ*, **802**, 20
 Scowcroft V., Freedman W. L., Madore B. F., Monson A. J., Persson S. E., Seibert M., Rigby J. R., Sturch L., 2011, *ApJ*, **743**, 76
 Scowcroft V., Freedman W. L., Madore B. F., Monson A., Persson S. E., Rich J., Seibert M., Rigby J. R., 2015, preprint, (arXiv:1502.06995)
 Skrutskie M. F., et al., 2006, *AJ*, **131**, 1163
 Sollima A., Borissova J., Catelan M., Smith H. A., Minniti D., Cacciari C., Ferraro F. R., 2006, *ApJ*, **640**, L43
 Stetson P. B., 1987, *PASP*, **99**, 191
 Stetson P. B., 1994, *PASP*, **106**, 250
 Villanova S., et al., 2007, *ApJ*, **663**, 296
 Villanova S., Geisler D., Gratton R. G., Cassisi S., 2014, *ApJ*, **791**, 107

APPENDIX A: RRL PHOTOMETRY

Table A1: JHK_s , 3.6 μm , and 4.5 μm photometry of the RRLs in ω Cen

ID	RA (J2000)	Dec (J2000)	Mode	P (days)	J	σ_J	H	σ_H	K_s	σ_{K_s}	[3.6]	$\sigma_{[3.6]}$	$\Delta[3.6]$	[4.5]	$\sigma_{[4.5]}$	$\Delta[4.5]$	[Fe/H], p	$\sigma_{[\text{Fe/H}]}, \text{p}$	[Fe/H], s	$\sigma_{[\text{Fe/H}]}, \text{s}$
3	13:25:56.15	-47:25:53.8	RRab	0.841	13.247	0.017	12.982	0.018	12.882	0.017	12.841	0.039	-0.086	12.708	0.036	0.031	-1.540	0.050	—	—
4	13:26:12.93	-47:24:18.8	RRab	0.627	13.475	0.016	13.219	0.021	13.133	0.020	13.030	0.036	0.027	13.026	0.035	0.013	-1.740	0.050	—	—
5	13:26:18.33	-47:23:12.4	RRab	0.515	13.700	0.017	13.549	0.020	13.507	0.027	13.387	0.043	-0.128	13.340	0.030	-0.100	-1.350	0.080	-1.240	0.110
7	13:27:00.90	-47:14:00.5	RRab	0.713	13.333	0.009	13.151	0.031	13.036	0.018	—	—	—	—	—	—	-1.460	0.080	—	—
8	13:27:48.45	-47:28:20.3	RRab	0.521	13.505	0.015	13.258	0.017	13.223	0.014	—	—	—	—	—	—	-1.910	0.280	—	—
9	13:25:59.58	-47:26:24.0	RRab	0.523	13.776	0.017	13.534	0.021	13.470	0.016	13.315	0.036	-0.071	13.279	0.039	-0.055	-1.490	0.060	—	—
11	13:26:30.59	-47:23:01.6	RRab	0.565	13.481	0.014	13.307	0.028	13.219	0.025	13.050	0.058	—	—	—	—	-1.670	0.130	-1.610	0.220
13	13:25:58.18	-47:25:21.6	RRab	0.669	13.353	0.019	13.081	0.022	13.058	0.017	12.918	0.032	0.073	12.860	0.031	0.114	-1.910	0.000	—	—
14	13:25:59.74	-47:39:09.6	RRc	0.377	13.588	0.011	13.343	0.020	13.365	0.016	—	—	—	13.299	0.045	—	-1.710	0.130	—	—
15	13:26:27.11	-47:24:38.0	RRab	0.811	13.245	0.018	13.020	0.031	12.954	0.025	13.149	0.084	—	—	—	—	-1.640	0.390	-1.680	0.180
16	13:27:37.69	-47:37:34.8	RRc	0.330	13.680	0.015	13.502	0.022	13.437	0.018	—	—	—	—	—	—	-1.290	0.080	-1.650	0.460
18	13:27:45.11	-47:24:56.6	RRab	0.622	13.371	0.010	13.131	0.024	13.100	0.016	13.006	0.043	—	—	—	—	-1.780	0.280	—	—
20	13:27:14.05	-47:28:06.3	RRab	0.616	13.410	0.015	13.210	0.036	13.125	0.025	13.060	0.039	0.017	12.940	0.029	0.119	—	—	-1.520	0.340
21	13:26:11.17	-47:25:58.8	RRc	0.381	13.578	0.016	13.399	0.027	13.361	0.020	13.301	0.047	-0.003	13.200	0.032	0.061	-0.900	0.110	—	—
23	13:26:46.50	-47:24:39.5	RRab	0.511	13.941	0.025	13.794	0.048	13.658	0.033	13.325	0.064	—	—	—	—	-1.080	0.140	-1.350	0.580
30	13:26:15.94	-47:29:56.0	RRc	0.404	13.521	0.021	13.287	0.046	13.251	0.030	13.188	0.047	0.041	13.071	0.060	0.112	-1.750	0.170	-1.620	0.280
32	13:27:03.32	-47:21:38.9	RRab	0.620	13.508	0.009	13.244	0.018	13.132	0.018	—	—	—	—	—	—	-1.530	0.160	—	—
33	13:25:51.60	-47:29:05.8	RRab	0.602	13.338	0.015	13.106	0.022	13.091	0.019	—	—	—	13.006	0.035	—	-2.090	0.230	-1.580	0.420
34	13:26:07.21	-47:33:10.4	RRab	0.734	13.273	0.014	13.018	0.044	12.916	0.013	—	—	—	12.838	0.065	—	-1.710	0.000	—	—
35	13:26:53.21	-47:22:34.7	RRc	0.387	13.586	0.012	13.463	0.024	13.356	0.023	—	—	—	—	—	—	-1.560	0.080	-1.630	0.360
36	13:27:10.11	-47:15:29.8	RRc	0.380	13.534	0.007	13.372	0.019	13.307	0.014	—	—	—	—	—	—	-1.490	0.230	—	—
38	13:27:03.30	-47:36:30.2	RRab	0.779	13.226	0.015	12.943	0.019	12.814	0.018	—	—	—	—	—	—	-1.750	0.180	-1.640	0.400
39	13:27:59.77	-47:34:42.3	RRc	0.393	13.560	0.009	13.415	0.014	13.308	0.014	—	—	—	—	—	—	-1.960	0.290	—	—
40	13:26:24.56	-47:30:46.2	RRab	0.634	13.517	0.022	13.250	0.051	13.153	0.033	13.062	0.049	-0.016	13.416	0.056	-0.388	-1.600	0.080	-1.620	0.190
44	13:26:22.39	-47:34:55.8	RRab	0.568	13.677	0.014	13.425	0.023	13.368	0.018	—	—	—	13.132	0.036	—	-1.400	0.120	-1.290	0.350
45	13:25:30.88	-47:27:21.0	RRab	0.589	13.513	0.015	13.201	0.015	13.164	0.014	—	—	—	13.070	0.028	—	-1.780	0.250	—	—
46	13:25:30.23	-47:25:51.8	RRab	0.687	13.299	0.016	12.998	0.017	12.947	0.014	—	—	—	—	—	—	-1.880	0.170	—	—
47	13:25:56.46	-47:24:12.0	RRc	0.485	13.420	0.020	13.223	0.018	13.150	0.018	13.099	0.030	-0.080	13.073	0.026	-0.126	-1.580	0.310	—	—
49	13:26:07.78	-47:37:55.5	RRab	0.605	13.566	0.012	13.238	0.019	13.220	0.016	—	—	—	13.099	0.049	—	-1.980	0.110	—	—
51	13:26:42.66	-47:24:21.4	RRab	0.574	13.597	0.014	13.378	0.033	13.270	0.029	13.315	0.083	—	—	—	—	-1.640	0.210	-1.840	0.230
54	13:26:23.54	-47:18:47.7	RRab	0.773	13.281	0.016	12.998	0.017	12.954	0.015	12.799	0.030	—	—	—	—	-1.660	0.120	-1.800	0.230
56	13:25:55.53	-47:37:44.1	RRab	0.568	13.643	0.009	13.386	0.022	13.353	0.017	—	—	—	13.232	0.035	—	-1.260	0.150	—	—
57	13:27:49.38	-47:36:50.5	RRab	0.794	13.234	0.015	12.995	0.018	12.882	0.014	—	—	—	—	—	—	-1.890	0.140	—	—
59	13:26:18.43	-47:29:46.7	RRab	0.519	13.727	0.023	13.424	0.043	13.391	0.033	13.248	0.071	0.005	13.418	0.064	-0.184	-1.000	0.280	—	—
63	13:25:07.96	-47:36:54.1	RRab	0.826	13.223	0.017	12.862	0.017	12.869	0.012	—	—	—	—	—	—	-1.730	0.090	—	—
64	13:26:02.22	-47:36:19.2	RRc	0.344	13.638	0.013	13.438	0.022	13.407	0.022	—	—	—	13.314	0.044	—	-1.460	0.230	—	—
67	13:26:28.62	-47:18:46.9	RRab	0.564	13.610	0.014	13.384	0.016	13.326	0.015	13.368	0.047	—	—	—	—	-1.100	0.000	-1.190	0.230
68	13:26:12.80	-47:19:35.7	RRc	0.535	13.258	0.021	13.004	0.015	12.970	0.015	12.928	0.050	—	—	—	—	-1.600	0.010	—	—
69	13:25:11.02	-47:37:33.5	RRab	0.635	—	—	—	—	13.112	0.014	—	—	—	—	—	—	-1.520	0.140	—	—
70	13:27:27.76	-47:33:42.7	RRc	0.391	13.529	0.013	13.282	0.029	13.254	0.022	—	—	—	—	—	—	-1.940	0.150	-1.740	0.300
72	13:27:33.11	-47:16:22.9	RRc	0.385	13.554	0.010	13.339	0.017	13.311	0.014	—	—	—	—	—	—	-1.320	0.220	—	—
73	13:25:53.75	-47:16:10.8	RRab	0.575	13.480	0.018	13.251	0.017	13.215	0.016	—	—	—	—	—	—	-1.500	0.090	—	—
74	13:27:07.22	-47:17:33.9	RRab	0.503	13.622	0.008	13.457	0.016	13.405	0.015	—	—	—	—	—	—	-1.830	0.360	—	—
75	13:27:19.70	-47:18:46.5	RRc	0.422	13.410	0.011	13.175	0.028	13.137	0.025	—	—	—	—	—	—	-1.490	0.080	-1.820	0.990
76	13:26:57.23	-47:20:07.7	RRc	0.338	13.634	0.012	13.488	0.017	13.449	0.020	—	—	—	—	—	—	-1.450	0.130	—	—
79	13:28:24.99	-47:29:25.2	RRab	0.608	13.382	0.010	13.162	0.016	13.123	0.015	—	—	—	—	—	—	-1.390	0.180	—	—
81	13:27:36.68	-47:24:48.3	RRc	0.389	13.542	0.013	13.326	0.033	13.286	0.025	13.248	0.076	—	—	—	—	-1.720	0.310	-1.990	0.430
82	13:27:35.61	-47:26:30.3	RRc	0.336	13.579	0.016	13.324	0.024	13.296	0.018	—	—	—	13.827	0.104	—	-1.560	0.200	-1.710	0.560
83	13:27:08.42	-47:21:34.1	RRc	0.357	13.603	0.010	13.431	0.024	13.370	0.022	—	—	—	—	—	—	-1.300	0.220	—	—
84	13:24:47.45	-47:29:56.5	RRab	0.580	—	—	12.833	0.017	12.781	0.016	—	—	—	—	—	—	-1.470	0.100	—	—
85	13:25:06.49	-47:23:34.0	RRab	0.743	13.344	0.011	—	—	—	—	—	—	—	—	—	—	-1.870	0.310	—	—
94	13:25:57.06	-47:22:46.1	RRc	0.254	14.070	0.024	13.934	0.022	13.870	0.027	13.858	0.038	-0.092	13.799	0.029	-0.014	-1.000	0.110	—	—
95	13:25:24.95	-47:28:53.2	RRc	0.405	13.497	0.015	13.269	0.017	13.264	0.017	—	—	—	13.178	0.024	—	-1.840	0.550	—	—
97	13:27:08.49	-47:25:30.9	RRab	0.692	13.302	0.010	13.143	0.029	13.034	0.022	12.964	0.061	-0.007	12.702	0.064	0.237	-1.560	0.370	-1.740	0.170
101	13:27:30.24	-47:29:51.0	RRc	0.341	13.708	0.016	13.484	0.030	13.436	0.023	—	—	—	—	—	—	-1.880	0.320	—	—
102	13:27:22.11	-47:30:12.3	RRab	0.691	13.320	0.012	13.033	0.022	12.993	0.020	12.984	0.049	-0.027	13.056	0.072	-0.116	-1.840	0.130	-1.650	0.160
103	13:27:14.29	-47:28:36.3	RRc	0.329	13.620	0.018	13.409	0.040	13.377	0.034	12.960	0.071	—	13.024	0.066	—	-1.920	0.110	-1.780	0.270
104	13:28:07.76	-47:33:44.9	RRab	0.867	13.732	0.096	13.626	0.154	13.452	0.141	—	—	—	—	—	—	-1.830	0.180	—	—
105	13:27:46.02	-47:32:43.9	RRc	0.335	13.768	0.014	13.615	0.020	13.533	0.018	—	—	—	—	—	—	-1.240	0.180	—	—

Table A1 - Continued from previous page

ID	RA (J2000)	Dec (J2000)	Mode	P (days)	J	σ_J	H	σ_H	K_s	σ_{K_s}	[3.6]	$\sigma_{[3.6]}$	$\Delta[3.6]$	[4.5]	$\sigma_{[4.5]}$	$\Delta[4.5]$	[Fe/H], p	$\sigma_{[\text{Fe/H}]}, p$	[Fe/H], s	$\sigma_{[\text{Fe/H}]}, s$
107	13:27:14.05	-47:30:57.9	RRab	0.514	13.597	0.017	13.340	0.038	13.301	0.030	13.535	0.219	–	13.351	0.076	–	-1.360	0.110	–	–
115	13:26:12.30	-47:34:17.5	RRab	0.630	13.401	0.012	13.176	0.017	13.103	0.013	–	–	–	–	–	–	-1.870	0.010	-1.640	0.320
117	13:26:19.91	-47:29:21.0	RRc	0.422	13.480	0.020	13.274	0.043	13.202	0.031	13.110	0.044	0.071	12.949	0.043	0.179	-1.680	0.250	–	–
120	13:26:25.52	-47:32:48.6	RRab	0.549	13.525	0.049	13.072	0.079	13.135	0.094	12.958	0.066	0.237	12.927	0.055	0.250	-1.390	0.060	-1.150	0.160
121	13:26:28.17	-47:31:50.5	RRc	0.304	13.741	0.016	13.648	0.033	13.531	0.026	13.414	0.037	0.144	13.302	0.033	0.249	-1.460	0.130	-1.830	0.400
122	13:26:30.31	-47:33:02.2	RRab	0.635	13.369	0.018	13.132	0.042	13.062	0.024	13.057	0.052	-0.012	13.019	0.043	0.008	-2.020	0.180	-1.790	0.210
122	13:26:30.31	-47:33:02.2	RRab	0.635	13.369	0.018	13.132	0.042	13.062	0.024	13.057	0.052	-0.012	12.956	0.105	0.071	-2.020	0.180	-1.790	0.210
124	13:26:54.49	-47:39:07.5	RRc	0.332	13.708	0.013	13.510	0.018	13.482	0.023	–	–	–	–	–	–	-1.330	0.230	–	–
125	13:26:48.92	-47:41:03.7	RRab	0.593	13.420	0.015	13.200	0.016	13.153	0.015	–	–	–	–	–	–	-1.670	0.220	-1.810	0.380
126	13:28:08.03	-47:40:46.7	RRc	0.342	13.642	0.011	13.467	0.017	13.370	0.016	–	–	–	–	–	–	-1.310	0.130	–	–
127	13:25:19.36	-47:28:37.6	RRc	0.305	–	–	–	–	13.579	0.018	–	–	–	13.573	0.063	–	-1.590	0.080	–	–
128	13:26:17.75	-47:30:13.0	RRab	0.835	13.207	0.018	12.927	0.032	12.810	0.020	–	–	–	12.445	0.074	–	-1.880	0.040	–	–
130	13:26:09.93	-47:13:40.0	RRab	0.493	13.688	0.021	13.527	0.032	13.418	0.025	–	–	–	–	–	–	-1.460	0.170	–	–
147	13:27:15.86	-47:31:09.2	RRc	0.423	13.397	0.012	12.934	0.041	13.083	0.022	–	–	–	12.585	0.096	–	-1.660	0.140	–	–
149	13:27:32.94	-47:13:43.6	RRab	0.683	13.354	0.015	13.061	0.035	13.024	0.024	–	–	–	–	–	–	-1.210	0.240	–	–
150	13:27:40.21	-47:36:00.1	RRab	0.899	13.068	0.019	12.757	0.025	12.692	0.018	–	–	–	–	–	–	-1.760	0.340	–	–
163	13:25:49.42	-47:20:21.5	RRc	0.313	13.763	0.019	13.557	0.016	13.545	0.025	–	–	–	–	–	–	-1.180	0.270	–	–
168	13:25:52.78	-47:32:02.9	RRc	0.321	14.176	0.015	14.000	0.020	13.960	0.018	–	–	–	–	–	–	–	–	–	–
169	13:27:20.47	-47:23:59.1	RRc	0.319	13.805	0.013	13.735	0.019	13.652	0.025	13.734	0.050	-0.232	14.001	0.116	-0.512	–	–	-1.650	0.190
184	13:27:28.50	-47:31:35.4	RRc	0.303	13.778	0.012	13.624	0.028	13.536	0.019	–	–	–	–	–	–	–	–	–	–
185	13:26:04.13	-47:21:45.0	RRc	0.333	13.701	0.016	13.545	0.018	13.508	0.023	13.496	0.036	-0.043	13.479	0.033	-0.046	–	–	–	–
261	13:27:15.41	-47:21:29.5	RRc	0.403	13.431	0.009	13.212	0.019	13.113	0.020	–	–	–	–	–	–	–	–	-1.500	0.350
263	13:26:13.13	-47:26:09.7	RRab	1.012	13.155	0.017	12.888	0.017	12.746	0.016	–	–	–	12.660	0.034	–	–	–	-1.730	0.190
274	13:26:43.73	-47:22:48.2	RRc	0.311	13.828	0.011	13.758	0.023	13.650	0.022	–	–	–	–	–	–	–	–	–	–
276	13:27:16.51	-47:33:17.6	RRc	0.308	13.727	0.021	13.614	0.046	13.533	0.024	–	–	–	–	–	–	–	–	–	–
280	13:27:09.33	-47:23:05.7	RRc	0.282	13.951	0.012	13.905	0.026	13.816	0.029	–	–	–	–	–	–	–	–	–	–
285	13:25:40.20	-47:34:48.4	RRc	0.329	13.687	0.017	13.504	0.027	13.503	0.015	–	–	–	13.358	0.074	–	–	–	–	–
288	13:28:10.32	-47:23:47.8	RRc	0.295	13.809	0.011	13.719	0.016	13.635	0.019	–	–	–	–	–	–	–	–	–	–
289	13:28:03.68	-47:21:27.9	RRc	0.308	13.743	0.013	13.618	0.015	13.584	0.022	–	–	–	–	–	–	–	–	–	–
357	13:26:17.77	-47:30:23.4	RRc	0.298	13.692	0.027	13.468	0.064	13.468	0.045	13.462	0.044	0.120	13.375	0.041	0.204	–	–	-1.640	0.990

This paper has been typeset from a \TeX/L\AA\TeX file prepared by the author.